THE SIZE EVOLUTION OF PASSIVE GALAXIES: OBSERVATIONS FROM THE WIDE FIELD CAMERA 3
EARLY RELEASE SCIENCE PROGRAM

R. E. Ryan Jr.[2], P. J. McCarthy[3], S. H. Cohen[4], H. Yan[5], N. P. Hathi[6], A. M. Koekemoer[7], M. J. Rutkowski[4], M. R. Mechtley[4], R. A. Windhorst[4], R. W. O'Connell[8], B. Balick[9], H. E. Bond[7], H. Bushouse[7], D. Calzetti[10], R. M. Crockett[11], M. Disney[12], M. A. Dopita[13], J. A. Frogel[14], D. N. B. Hall[15], J. A. Holtzman[16], S. Kaviraj[11], R. A. Kimble[17], J. MacKenty[7], M. Mutchler[7], F. Paresce[18], A. Saha[19], J. I. Silk[11], J. Trauger[20], A. R. Walker[21], B. C. Whitmore[7], and E. Young[22]

Draft version July 12, 2010

ABSTRACT

We present results on the size evolution of passively evolving galaxies at $1 \lesssim z \lesssim 2$ drawn from the Wide Field Camera 3 Early Release Science program. Our sample was constructed using an analog to the passive BzK selection criterion, which isolates galaxies with little or no on-going star formation at $z \gtrsim 1.5$. We identify 30 galaxies in ~ 40 arcmin^2 to $H < 25$ mag. We supplement spectroscopic redshifts from the literature with photometric redshifts determined from the 15-band photometry from $0.22 - 8$ μm. We determine effective radii from Sérsic profile fits to the H-band image using an empirical PSF. We find that size evolution is a strong function of stellar mass, with the most massive ($M_* \sim 10^{11}$ $M_\odot$) galaxies undergoing the most rapid evolution from $z \sim 2$ to the present. Parameterizing the size evolution as $(1 + z)^{-\alpha}$, we find a tentative scaling between α and stellar mass of $\alpha \approx -1.8 + 1.4 \log(M/10^9$ $M_\odot)$. We briefly discuss the implications of this result for our understanding of the dynamical evolution of the red galaxies.

Subject headings: Keywords: galaxies: evolution — galaxies: structure — galaxies: fundamental parameters

1. INTRODUCTION

Understanding the red, passively evolving, galaxies at intermediate redshifts ($z \sim 2$) is one of the outstand-

rryan@physics.ucdavis.edu
[2] Physics Department, University of California, Davis, CA 95616
[3] Observatories of the Carnegie Institute of Washington, Pasadena, CA 91101
[4] School of Earth and Space Exploration, Arizona State University, Tempe AZ 85287
[5] Center for Cosmology and Astroparticle Physics, Ohio State University, Columbus, OH 43210
[6] Department of Physics and Astronomy, University of California, Riverside, CA 92521
[7] Space Telescope Science Institute, Baltimore, MD 21218
[8] Department of Astronomy, University of Virginia, Charlottesville, VA 22904
[9] Department of Astronomy, University of Washington, Seattle, WA 98195
[10] Department of Astronomy, University of Massachusetts, Amherst, MA 01003
[11] Department of Physics, University of Oxford, Oxford OX1 3PU, United Kingdom
[12] School of Physics and Astronomy, Cardiff University, Cardiff CF24 3AA, United Kingdom
[13] Research School of Astronomy and Astrophysics, The Australian National University, Weston Creek, ACT 2611, Australia
[14] Association of Universities for Research in Astronomy, Washington, DC 20005
[15] Institute for Astronomy, University of Hawaii, Honolulu, HI 96822
[16] Department of Astronomy, New Mexico State University, Las Cruces, NM 88003
[17] NASA, Goddard Space Flight Center, Greenbelt, MD 20771
[18] Istituto di Astrofisica Spaziale e Fisicia Cosmica, INAF, via Gobetti 101, 40129 Bologna, Italy
[19] National Optical Astronomy Observatories, Tucson, AZ 85726
[20] NASA, Jet Propulsion Laboratory, Pasadena, CA 91109
[21] Cerro Tololo Inter-American Observatory, La Serena, Chile
[22] NASA, Ames Research Center, Moffett Field, CA 94035

ing challenges of galaxy evolution studies. Early expectations of a high luminosity phase associated with the formation of spheroids on a free-fall time scale (Eggen, Lynden-Bell, & Sandage 1962) have long given way to a framework in which the spheroids are assembled over an extended period of time. The identification of fairly high space densities of massive and passively evolving galaxies at $z \gtrsim 1.5$ (e.g. Glazebrook et al. 2004; Cimatti et al. 2004) revealed weaknesses in the early semi-analytic models of their formation. Large-scale surveys, both locally and out to $z \sim 1$, provide a fairly clear view of the evolution in the number density of red sequence galaxies and the global stellar mass density in passive systems (e.g. Bell et al. 2006; Faber et al. 2007; Brown et al. 2003, 2007).

Deep spectroscopic studies of red galaxies (e.g. McCarthy et al. 2004; Cimatti et al. 2006, 2008) estimated stellar ages consistent with early formation redshifts ($z_{\rm form} \gtrsim 4$), potentially at odds with the rapid evolution in stellar mass density at these epochs (e.g. Rudnick et al. 2003). It is now clear that the red sequence was in place at fairly early epochs (Bell et al. 2004; Bremer et al. 2006), but evolved strongly in the $1 \lesssim z \lesssim 3$ era (e.g. Demarco et al. 2010) and likely since $z \sim 1$ as well (e.g. Faber et al. 2007). The emerging picture in which massive galaxies are assembled via mergers followed by a rapid quenching of star formation addresses many of the salient properties of the red sequence galaxies (Faber et al. 2007).

In light of these results it was quite surprising that high spatial resolution studies showed that the passive red galaxies at intermediate redshifts are systematically smaller than their likely present-day counterparts (e.g. Daddi et al. 2005; Trujillo et al. 2006). Observations of $1 \lesssim z \lesssim 2$ passive galaxies with either Advanced Camera

of Surveys (ACS) or Near Infrared Camera and Multi-Object Spectrometer (NICMOS) on the *Hubble Space Telescope* (*HST*) gave sizes that are a factor of ~ 2 smaller than equal mass red galaxies today (e.g. Longhetti et al. 2007; Cimatti et al. 2008; Damjanov et al. 2009), while observations of red galaxies at $z \gtrsim 2$ suggest even more dramatic evolution (e.g. van Dokkum et al. 2008; Saracco, Longhetti, & Gargiulo 2010).

The primary interest in determining the characteristic sizes of passive galaxies is the insight that it provides into the dynamical state of the system. As one projection of the fundamental plane (Djorgovski & Davis 1987; Dressler et al. 1987), the Kormendy relation (Kormendy 1977) provides a probe of the dynamics of hot stellar systems. The Kormendy diagram for the $z \gtrsim 1$ red sequence galaxies is nearly as tight as it is locally, but is offset in both surface brightness and size (e.g. Damjanov et al. 2009), even when the effects of passive fading of the stellar populations is taken into account. The compact sizes and high surface brightness of the red galaxies implies stellar densities in the centers of these galaxies that are two to three orders of magnitude higher than present day massive red galaxies (e.g. van Dokkum et al. 2008; Damjanov et al. 2009).

The challenge in understanding these results stems from the apparent conflict between the requirement for a factor of ~ 3 growth in size during an epoch in which the stellar masses, population ages, and overall morphologies show little or no evolution. A number of models are under active discussion, but most involve large numbers of late stage minor mergers that grow the galaxies in size without contributing large amounts of mass. While it is difficult to conclusively rule out various measurement biases which might give rise to this apparent trend (e.g. underestimated effective radii or overestimated masses), most interpretations are astrophysical in origin: (major or minor) merging occurring at different phases (e.g. Naab, Khochfar, & Burkert 2006), or expansion due to a significant mass loss, either by an active galactic nucleus (Fan et al. 2008) or stellar winds (Damjanov et al. 2009). Recently Hopkins et al. (2010a) present a semi-analytic model based on high-resolution hydrodynamic simulations (Cox et al. 2006), which incorporates several astrophysical and observational mechanisms for this trend, and conclude that for galaxies with a stellar mass of $M_* \geq 10^{11} \ M_\odot$, the late-stage minor merging is the dominate mechanism, accounting for $\sim 50\%$ of the apparent size evolution. Certainly many of these high-redshift systems do in fact show merger-like features (e.g. van Dokkum 2005; van Dokkum & Brammer 2010) or have (multiple) companions (e.g. Bell et al. 2006).

The merging scenario implies that some non-negligible fraction ($\lesssim 10\%$; Hopkins et al. 2009) of compact galaxies should remain to $z \sim 0$. However Trujillo et al. (2009) find only 0.03% ($= 48/152,083$) galaxies at $z \sim 0.2$ have stellar densities comparable to these high redshift galaxies, arguing against the merger scenario. To further confound the issue, these galaxies are generally young (~ 3 Gyr old), giving an approximate formation redshift of $z_{\rm form} \sim 0.3$, suggesting that they are not the relics of the early universe, but formed from gas-rich, recently merged disks. Conversely, Saracco, Longhetti, & Gargiulo (2010) find that $\sim 62\%$ ($= 21/34$) of their galaxies at $1 < z_{\rm spec} < 2$ are within 1σ of the local $R_e - M_*$ relation (Shen et al. 2003). Based on this finding, they suggest that the compact high redshift galaxies are not the progenitors of large field galaxies, but of compact brightest cluster galaxies. The absence of compact early-type galaxies at $z \sim 0$ seems to suggest that the simple picture of galaxy merging with some mass-loss expansion is not completely correct, in stark contrast to the simulated results (e.g. Naab, Johansson, & Ostriker 2009; Hopkins et al. 2010a).

This paper is organized as follows. In § 2 we describe the observations and ancillary data, in § 3 we define our sample, in § 4 we detail our stellar population modeling and morphological analysis, in § 4 we describe our mass-dependent size evolution model, in § 6 we discuss several key results, and in § 7 we give a brief summary of this work with thoughts for future surveys. Throughout this paper we assume a ΛCDM cosmology with $\Omega_0 = 0.27$, $\Omega_\Lambda = 0.73$, and $H_0 = 73$ km s^{-1} Mpc^{-1} (Spergel et al. 2003) and will quote all magnitudes in the AB$_\nu$ magnitude system (Oke & Gunn 1983).

2. OBSERVATIONS

2.1. *The Wide Field Camera 3 Early Release Science*

For this work we analyze the Early Release Science (ERS; PropID: 11359, PI: R. W. O'Connell) observations conducted with the Wide-Field Camera 3 (WFC3) recently installed on the *Hubble Space Telescope* (*HST*). This field covers roughly the northern 40 arcmin^2 of the Great Observatories Origins Deep Survey southern field (GOODS-S; Giavalisco et al. 2004), and leverages the existing Advanced Camera for Surveys (ACS) optical data with near-ultraviolet (NUV) and near-infrared (NIR) data with equivalent space-based imaging. The main details regarding the data collection, reduction, calibration, and mosaicking are presented by Windhorst et al. (2010). We briefly summarize the observational aspects critical to this work.

The ERS program utilizes the two complementary modes of the WFC3: UVIS and IR channels. The data were collected between September and November 2009 and form a 2×4 and 2×5 mosaic, respectively. The final dataset consists of ~ 40 arcmin^2 of 10-band *HST* imaging covering 2250 Å to 1.6 μm in wavelength. The v2.0 GOODS high-level science products had an original pixel scale of 30 milliarcseconds, and were 3×3 block summed to produce science and weight maps of equal pixel scale to the WFC3 observations (see Windhorst et al. 2010, for a more detailed discussion on the rebinning process and its motivation). Therefore, our final *HST* mosaics have 90 milliarcsecond pixels. We refer hereafter to the 10-band WFC3 and ACS filter set in the F225W, F275W, F336W, F435W, F606W, F775W, F850LP, F098M, F125W, and F160W as $U_1 U_2 U_3 B V i' z' Y_s J H$ to simplify the bandpass notation.

2.2. *Source Catalogs*

We created source catalogs using SExtractor (Bertin & Arnouts 1996) with the H-band mosaic as the detection image and each of the *HST* mosaics as measurement images. We use the weight maps produced by MultiDrizzle (Koekemoer et al. 2002), modified to ac-

count for correlated pixel noise (Dickinson et al. 2004). For object detection, we require a minimum of 5 connected pixels each greater than 0.6σ above the local background and apply a 3 pixel Gaussian smoothing filter. For deblending, we adopt a contrast parameter of 10^{-4} with 64 sub-thresholds. For photometry, we adopt the `MAG_AUTO` measurements with a Kron factor of 2.5, and minimum object radius of 3.5 pixels, which reliably recover total fluxes to within $\sim 6\%$ (Bertin & Arnouts 1996). We use the AB zeropoints given by Kalirai et al. (2009a,b) for the UVIS and IR data, respectively.

3. SAMPLE SELECTION

We select our passively evolving galaxies using a variation on the standard $pBzK$ selection (Daddi et al. 2004), designed to identify galaxies at $z\sim 2$ with little on-going star formation and stellar population ages of ~ 1 Gyr (Daddi et al. 2005). However, to take full advantage of our high-spatial resolution and significantly deeper ERS dataset, we use our H-band imaging instead of the ground-based K-band images. Therefore we modify the classical $pBzK$ selection criteria to an equivalent $pBzH$ scheme:

$$(z'-H)-(B-z') < -0.2-\langle(H-K)\rangle \text{ mag}, \quad (1)$$
$$(z'-H) > 2.5-\langle(H-K)\rangle \text{ mag}. \quad (2)$$

As these $pBzK$ galaxies have maximally-old, passively evolving systems, we derive a typical $\langle(H-K)\rangle$ color indicative of a stellar population with an instantaneous star-formation history formed at $z_{\rm form}=10$ based on the Charlot & Bruzual (2007, hereafter CB07) models of $\langle(H-K)\rangle = 0.7$ mag. In Figure 1, we show the $(B-z')$ and $(z'-H)$ colors with these criteria illustrated as a shaded polygon. To rule out any potential image artifacts associated with the ERS field edges, we require the objects to be in the portion of the H-band mosaic which received the full complement of two orbits per pointing. We restrict the H-band magnitude to a relatively conservative limit of $H \leq 25$ mag to ensure a complete and reliable sample (Windhorst et al. 2010). With these requirements, we identify a final sample of 30 galaxies in 43.1 arcmin^2. Of these galaxies, 15 objects have $(B-z')$ colors redder than the plot limits and are not represented in Figure 1. We tabulate the 30 candidates in Table 1 and show color stamps of each object in Figure 2.

We show the source counts of BzH galaxies in Figure 3. The counts plateau around $H \simeq 22.5$ mag, which is roughly 4 mag *brighter* than the formal ERS completeness limit (Windhorst et al. 2010), suggesting that the faint-end of their luminosity function is relatively flat or declining. At the bright-end ($H \lesssim 22$ mag), our survey and modified $pBzK$ selection method produces source counts consistent with Lane et al. (2007), based on the UKIRT Infrared Deep Sky Survey (UKIDSS) Ultra Deep Survey (UDS). While the UKIDSS/UDS survey is much wider (~ 0.6 deg^2), the ERS data pushes $\gtrsim 2$ AB mag deeper, into a regime not routinely possible from the ground.

4. ANALYSIS

4.1. *Surface Brightness Models*

To determine the rest frame optical morphologies of our galaxies, we model the two dimensional light distri-
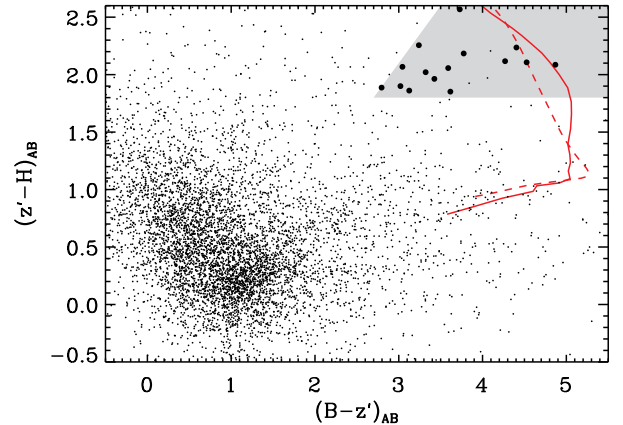

FIG. 1.— The BzH object selection. The small dots represent all objects detected and measured by `SExtractor`. The grey area is the color selection region defined by equations 1 and 2 with a typical color of $\langle(H-K)\rangle = 0.7$ mag. We identify 30 galaxies strictly meeting the BzH color criteria (shown as large filled circles), however 15 galaxies have $(B-z')$ colors too red to be shown here. There are several galaxies which formally meet our color criteria but were rejected as being too faint or too close to survey edges to be studied. The red lines show the tracks for the Coleman, Wu, & Weedman (1980, dashed) and Charlot & Bruzual (2007, solid) templates. We note, Galactic stars will span roughly similar $(B-z')$ colors but will be $\gtrsim 0.7$ mag too blue in $(z'-H)$ to have been misidentified as BzH galaxies (see also Daddi et al. 2004).

bution in the H-band using `GalFit` (Peng et al. 2002). We determine an empirical point-spread function (PSF) from a median stack of 75 stars identified in the field, based on their full-width at half-maximum (FWHM) and brightness determined by `SExtractor` (Windhorst et al. 2010). We fit the standard Sérsic profile:

$$\Sigma(r) = \Sigma_e \, e^{-b_n[(r/r_e)^n-1]}, \quad (3)$$

where r_e is the effective radius[22], Σ_e is the surface brightness at the effective radius, n is the Sérsic index, and b_n is a constant found by numerically solving $\Gamma(2n) = 2\gamma(2n, b_n)$. Since `GalFit` is minimizing a goodness-of-fit, modeling the uncertainty in each pixel is critical for meaningful estimate of the uncertainty in each of the fit parameters. Therefore, we transform the weight maps produced by `MultiDrizzle` to uncertainty maps and explicitly include the shot noise of the objects. We perform all fits with `GalFit` in units of counts using the H-band mosaic effective exposure time of 5017.7 seconds.

We excise a 81 pix $\times$ 81 pix stamp centered on each galaxy; this size was chosen as a compromise between a sufficient number of sky pixels for a robust sky estimation by `GalFit`, and the number of (generally unassociated) nearby galaxies. Neighboring galaxies can bias the parameter estimation of the primary galaxy, therefore one must carefully mask out the unmodeled objects, or simultaneously fit all the objects in the stamp. We opt for the latter, since it avoids the ambiguities in pixel masking, and permits the flux in a given pixel to be represented as the sum of several independent components. However without good initial conditions, the `GalFit` algorithm

---

[22] We refer to the effective radius as r_e when in angular units and as R_e when converted to physical units.

TABLE 1
BzH Sample and HST Photometry

ID	RA[†] (h m s)	Dec[†] (° ′ ″)	B (mag)	V (mag)	i′ (mag)	z′ (mag)	Y_s (mag)	J (mag)	H (mag)	Notes
408	3 32 28.02	−27 40 31.2	27.52 ± 0.49	26.18 ± 0.12	25.18 ± 0.08	24.40 ± 0.05	23.77 ± 0.03	22.87 ± 0.01	22.54 ± 0.01	· · ·
606	3 32 23.27	−27 40 45.8	> 28.11	27.60 ± 0.53	26.12 ± 0.23	25.36 ± 0.14	25.16 ± 0.17	23.66 ± 0.03	23.10 ± 0.02	· · ·
1696	3 32 42.08	−27 41 41.2	> 27.36	> 27.29	26.69 ± 1.12	26.16 ± 0.77	25.47 ± 0.32	24.98 ± 0.14	24.08 ± 0.08	· · ·
2227	3 32 42.34	−27 42 04.0	> 27.55	26.85 ± 0.63	24.53 ± 0.13	24.50 ± 0.14	23.86 ± 0.07	22.91 ± 0.02	22.32 ± 0.01	· · ·
2377	3 32 25.03	−27 42 09.6	> 28.10	27.80 ± 0.67	27.68 ± 1.04	27.43 ± 1.00	26.44 ± 0.42	25.42 ± 0.11	24.52 ± 0.06	X-ray ID 226[‡]
2749	3 32 14.92	−27 42 21.9	> 27.23	26.40 ± 0.44	24.92 ± 0.19	24.64 ± 0.19	24.67 ± 0.19	23.22 ± 0.03	22.69 ± 0.03	· · ·
2750	3 32 14.88	−27 42 23.3	> 27.26	25.70 ± 0.22	24.56 ± 0.14	23.92 ± 0.09	23.95 ± 0.09	22.46 ± 0.02	21.97 ± 0.01	X-ray ID 145[‡]
2871	3 32 31.09	−27 42 26.6	> 28.23	26.85 ± 0.22	25.78 ± 0.14	24.91 ± 0.08	24.17 ± 0.05	23.39 ± 0.02	23.07 ± 0.02	· · ·
3000	3 32 43.93	−27 42 32.4	26.23 ± 0.47	25.12 ± 0.13	23.61 ± 0.06	22.64 ± 0.03	21.99 ± 0.02	21.07 ± 0.00	20.59 ± 0.00	· · ·
3152	3 32 26.05	−27 42 36.6	> 27.96	27.21 ± 0.44	24.93 ± 0.09	23.93 ± 0.05	23.31 ± 0.02	22.15 ± 0.01	21.66 ± 0.00	· · ·
3237	3 32 35.91	−27 42 40.9	> 28.04	26.77 ± 0.30	25.24 ± 0.13	24.60 ± 0.08	23.90 ± 0.05	22.67 ± 0.01	22.06 ± 0.01	· · ·
3360	3 32 30.58	−27 42 43.4	> 28.06	27.27 ± 0.44	25.90 ± 0.22	24.65 ± 0.08	24.11 ± 0.05	22.78 ± 0.01	22.22 ± 0.01	· · ·
3376	3 32 35.13	−27 42 37.0	> 28.04	27.95 ± 0.74	26.80 ± 0.45	26.69 ± 0.48	25.40 ± 0.16	24.91 ± 0.07	24.55 ± 0.06	· · ·
3471	3 32 27.94	−27 42 45.7	28.29 ± 1.34	26.29 ± 0.17	24.75 ± 0.07	24.02 ± 0.04	23.48 ± 0.02	22.35 ± 0.01	21.91 ± 0.00	· · ·
3488	3 32 25.65	−27 42 46.8	> 27.97	> 28.20	> 27.63	26.95 ± 0.70	26.01 ± 0.31	25.38 ± 0.12	24.93 ± 0.10	· · ·
3551	3 32 36.28	−27 42 49.4	27.78 ± 1.42	26.05 ± 0.24	24.32 ± 0.08	23.38 ± 0.04	22.78 ± 0.02	21.63 ± 0.00	21.14 ± 0.00	· · ·
3812	3 32 36.66	−27 42 58.5	> 28.02	26.05 ± 0.15	24.87 ± 0.09	23.75 ± 0.04	23.35 ± 0.02	22.23 ± 0.01	21.74 ± 0.00	· · ·
4148	3 32 44.97	−27 43 09.1	27.33 ± 0.48	25.00 ± 0.05	24.43 ± 0.05	24.09 ± 0.04	23.82 ± 0.03	22.63 ± 0.01	21.83 ± 0.00	· · ·
4173	3 32 41.24	−27 43 09.7	> 27.57	26.31 ± 0.30	25.24 ± 0.19	24.48 ± 0.11	23.91 ± 0.07	23.29 ± 0.03	22.65 ± 0.02	· · ·
4324	3 32 31.32	−27 43 16.1	> 27.48	26.23 ± 0.29	24.65 ± 0.12	23.85 ± 0.07	23.23 ± 0.04	22.25 ± 0.01	21.77 ± 0.01	· · ·
4327	3 31 59.71	−27 43 15.5	> 28.40	28.48 ± 1.29	26.81 ± 0.47	26.89 ± 0.61	25.90 ± 0.36	25.47 ± 0.17	24.37 ± 0.08	· · ·
4534	3 32 29.99	−27 43 22.7	> 28.07	27.44 ± 0.51	25.42 ± 0.13	24.37 ± 0.06	23.84 ± 0.04	22.74 ± 0.01	22.26 ± 0.01	· · ·
4648	3 32 26.10	−27 43 26.7	28.39 ± 1.28	26.60 ± 0.23	25.47 ± 0.13	24.77 ± 0.08	24.29 ± 0.07	23.49 ± 0.02	22.92 ± 0.02	· · ·
4846	3 32 25.93	−27 43 31.1	> 28.28	> 28.37	26.45 ± 0.31	26.23 ± 0.31	25.28 ± 0.17	24.08 ± 0.04	23.67 ± 0.03	· · ·
4921	3 32 02.44	−27 43 35.8	> 28.03	> 28.14	> 27.58	26.98 ± 0.75	27.88 ± 1.69	26.13 ± 0.23	24.91 ± 0.10	· · ·
5410	3 32 32.11	−27 43 55.3	> 27.22	26.33 ± 0.38	25.26 ± 0.24	25.83 ± 0.50	25.53 ± 0.43	23.87 ± 0.06	23.45 ± 0.05	· · ·
5529	3 32 01.77	−27 44 01.1	27.56 ± 0.88	28.02 ± 1.16	25.76 ± 0.24	24.76 ± 0.12	24.39 ± 0.09	23.46 ± 0.03	22.87 ± 0.02	· · ·
5685	3 32 12.78	−27 44 07.7	27.98 ± 1.78	27.70 ± 1.10	25.17 ± 0.18	24.95 ± 0.18	24.17 ± 0.09	23.44 ± 0.03	23.06 ± 0.03	· · ·
5735	3 32 02.83	−27 44 09.7	> 28.05	26.80 ± 0.29	26.88 ± 0.52	26.52 ± 0.45	26.10 ± 0.33	25.80 ± 0.17	24.66 ± 0.08	· · ·
6845	3 32 06.57	−27 45 14.0	> 27.57	27.81 ± 1.15	25.93 ± 0.34	25.06 ± 0.18	24.80 ± 0.15	23.44 ± 0.03	22.69 ± 0.02	· · ·
7202	3 32 06.40	−27 45 54.7	27.10 ± 0.61	25.76 ± 0.15	24.78 ± 0.10	23.67 ± 0.05	23.16 ± 0.03	22.37 ± 0.01	21.71 ± 0.01	X-ray ID 82[‡]

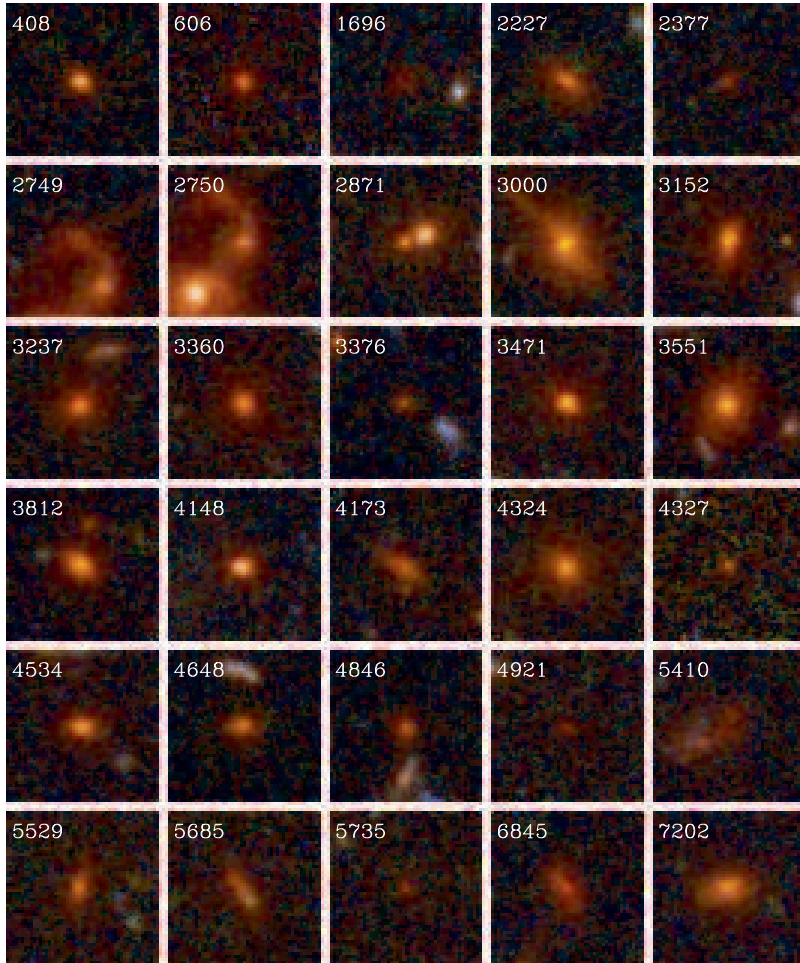[†]Coordinates refer to the J2000 epoch.

FIG. 2.— BzH color images. Each stamp is $\approx 4''.5$ (≈ 38 kpc at $z = 1.6$) on a side, has north up and east left, and has a pixel scale of $0''.090$ pix^{-1}. All images are shown with the same color and logarithmic intensity scale. We find the object just to the south of #2750 (and #2749) is just barely too blue to have been included in our sample, which is consistent with the suggestion that this object has recently (~ 150 Myr) undergone an intense burst of star formation of $500 - 2000$ $M_\odot$ yr^{-1} (van Dokkum & Brammer 2010).
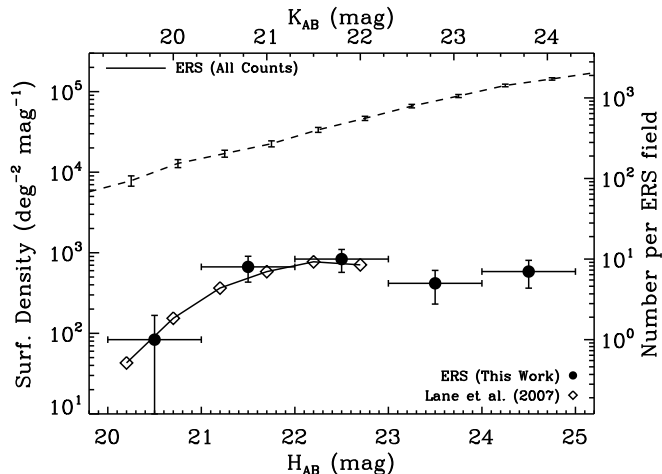
FIG. 3.— BzH galaxy counts. We show the differential surface density of galaxies selected based on the usual BzK color criteria (Daddi et al. 2004) and a typical color of $\langle (H-K) \rangle = 0.7$ mag, assuming an instantaneous burst of star formation and passive evolution from $z_{\rm form} = 10$. For comparison, we show the BzK object counts from Lane et al. (2007) from the UKIDSS/UDS survey as open symbols, which were derived from a strict BzK selection. The upper axis is simply a transformation using the assumed $\langle (H-K) \rangle$ color and the right axis applies to our objects. To demonstrate that the apparent plateau in the BzH counts $H_{\rm AB} \sim 22$ mag is not due to simple survey completeness, we show the total source counts from the ERS data as a dashed line (Windhorst et al. 2010). The uncertainties presented here reflect the Poisson variation in the object counts, and do not include any contribution from cosmic variance.

may not converge to a meaningful solution, since the number of degrees-of-freedom can be very large. Therefore, to estimate better initial conditions for each galaxy in the stamp and ultimately ensure convergence in the final simultaneous solution, we fit the two-dimensional light profiles of the primary BzH galaxy in question and any neighboring galaxies in a multi-stage process as follows:

1. We identify all neighboring galaxies and their associated pixels with `SExtractor`, using the same settings mentioned in § 2.2. Any sources with `FWHM_IMAGE`$_H \leq 1$ are eliminated from the `SExtractor` segmentation maps and object catalogs, since they are likely not galaxies.

2. The pixels of any galaxy whose isophotes are truncated (based on the `SExtractor` flags) are masked, by setting the uncertainty maps to 10^{10} ADU. These galaxies are no longer considered in the `GalFit` process.

3. We model the light distribution of each remaining galaxy (including the primary BzH galaxy) individually, while masking all the pixels associated with every other galaxy. For any neighboring galaxy with semi-minor axis of `B_IMAGE`$_H \leq 1$ pix from `SExtractor`, we switch from fitting a Sérsic profile to a PSF model, in order to eliminate degenerate degrees of freedom. Our results are robust to the choice of semi-minor axis limit, provided that we do not permit it to be larger than the size of the empirical PSF (discussed in more detail below). It is important to note that this step is only present to

get reasonably accurate initial conditions for subsequent simultaneous object fitting.

4. We refit a `GalFit` model, which contains a combination of point sources and Sérsic profiles, to the stamp as a whole using the results from the previous step as the initial guesses.

In a few cases, we manually masked diffraction spikes or stellar halos clearly associated with foreground stars, which were just outside the field-of-view of the stamp before proceeding through the above procedure.

For the individual and simultaneous fits, we placed constraints on various `GalFit` parameters to the algorithm from diverging into an unphysical regime. We constrained the centroid of any component to be within the $\pm 2\sigma$ of the centroid determined by `SExtractor`, and the total magnitude to be $35 \leq H_{\rm tot} \leq$ `MAG_AUTO`$_H - 2$ mag. In general, these constraints are so weak that they generally play no role in the fitting whatsoever, but they reduce the sensitivity to the pixel masking with the segmentation maps. We additionally constrain the Sérsic index and effective radius to be $0.01 \leq n \leq 8$ and $0.01 \leq r_e/$`A_IMAGE`≤ 5, respectively. These constraints are considerably stronger, and we recognize that the model is likely incorrect when `GalFit` converges to a solution which is on these boundaries. These cases are rare, and generally a sign that additional astrophysical components are needed (e.g. bulge/disk separately, nuclear point sources, or merger signatures), that the frame was inappropriately sized, that the object was unresolved, and/or that there was some additional light component or image defect present in the image (e.g. diffraction spikes, stellar halos, and/or cosmic rays).

As our primary interest here is on the sizes of these galaxies, it is imperative that we ensure the effective radii are robustly measured. While `GalFit` reliably determines the random uncertainty which follows from the maximum likelihood analysis, the total uncertainty should include a systematic term as well. To estimate the contribution from the systematic uncertainty, we construct a grid of simulated galaxies with brightnesses $20 \leq H \leq 25$ mag, effective radii $0.5 \leq r_e \leq 5.5$ pix, and a fixed Sérsic index of $n = 4$. These galaxies are convolved with the PSF and embedded in a blank region of the H-band mosaic. We then fit these simulated galaxies with `GalFit` using the above procedure, and find that the effective radii are generally uncertain by $\sim 10\%$, which is somewhat brightness dependent. We quadratically add this systematic uncertainty to the random uncertainty determined by `GalFit`.

Many of the these red galaxies are very small and, even with the space based imaging, may still be unresolved. Therefore it is critical to properly identify which galaxies are resolved and have reliable effective radii measurements. We begin by swapping the fully variable Sérsic model for the primary galaxy with a pure PSF model, which can only vary in position and brightness. However, as we have simultaneously fit every object in our postage stamps, we anticipate that `GalFit` may incorrectly change the parameters of neighboring (unrelated) galaxies to compensate for the poor primary model, particularly in the case of a well resolved primary galaxy. Therefore, when we use the PSF model for the primary
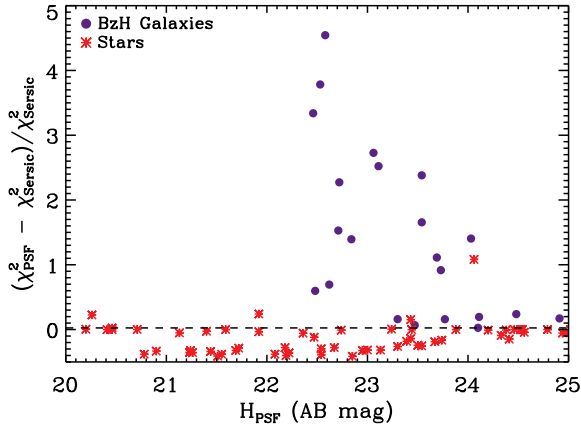
Fig. 4.— Comparison of PSF and Sérsic models. We show the fractional difference between the χ^2 goodness-of-fit measures from `GalFit` for the PSF and Sérsic models. The BzH galaxies are shown as filled blue points, while the red asterisks represent 75 ERS point sources, presumed to be stars. For `GalFit` to optimally fit an unresolved source with a PSF, it will drive the effective radius and Sérsic index to unphysical regimes, *de facto* fitting a PSF. Therefore, the goodness-of-fit of a Sérsic model and a PSF should be roughly equal. However, if one were to fit a PSF to a resolved object, then there should be a noticeable increase in the goodness-of-fit statistic. We adopt a critical value of $F_{\rm crit} = 0.01$ (Bond et al. 2009), see § 4.1 for more details. Of the 75 stars used in this test, only 4 have $F > F_{\rm crit}$ suggesting this is reliable way to classify unresolved objects.

galaxy, we hold the parameters of the neighboring sources fixed at the values found previously by `GalFit`. We now compare the goodness-of-fit statistics for these Sérsic and PSF models by considering the quantity:

$$F = \frac{\chi^2_{\rm PSF} - \chi^2_{\rm Sérsic}}{\chi^2_{\rm Sérsic}}, \quad (4)$$

and expect that sources with low values of F are equally well characterized by a PSF model as by the more complex Sérsic profile. We calibrate this quantity by computing the F-values of the known ERS stars, which were used to derive the empirical PSF used above. In Figure 4, we show the F-values as a function of the `GalFit`-derived PSF magnitude, with the galaxies plotted as filled-blue points and the stars as red asterisks. The trend is as expected: nearly all Galactic stars can be found at $-0.5 \lesssim F \lesssim 0$, while the BzH galaxies are generally at $F \gtrsim 0$ which depends on brightness. Therefore, we define objects which can be equally characterized by a PSF as by a Sérsic fit as having $F \leq F_{\rm crit}$, while objects with $F > F_{\rm crit}$ are more extended than the known ERS stars. We adopt $F_{\rm crit} = 0.025$ and note that only 4/75 stars have $F > F_{\rm crit}$, which is consistent with Bond et al. (2009). We give the `GalFit` results in Table 2.

4.2. *Additional Photometry*

Our BzH criteria are designed to select passively evolving galaxies at $z \sim 1.5$, consequently the *HST* photometry covers only $\lambda_{\rm rest} \lesssim 6000$ Å. We can extend our wavelength coverage to $\lambda_{\rm rest} \sim 3$ μm with the K_s-band imaging from the *Very Large Telescope* (*VLT*; Retzlaff et al. 2010) and the four IRAC channels from the *Spitzer Space Telescope* (*Spitzer*; PI: M. Dickinson).

However the notably lower spatial resolution ($0.''7 - 2''$) of these images demands a different approach for measuring the flux, as source confusion can significantly bias the photometry.

By inspection of the images, it is clear that our galaxies are unresolved in the *VLT* and *Spitzer* data. Therefore, we obtain total magnitudes from a `GalFit` model with a similar approach discussed in § 4.1, with a few simplifications. First, we assume that all the sources in a given postage stamp are unresolved, and are therefore ideally modeled by a PSF. Second, we do not allow the centroids of all objects to vary more than ± 1 pix (of the *VLT* or *Spitzer* images). Third, we only perform simultaneous fitting with initial magnitudes given by the H-band measurements, as in many cases multiple *HST* sources are blended into a single *VLT* or *Spitzer* source.

4.3. *Stellar Populations and Photometric Redshifts*

We fit the 15-band (*HST*, *VLT*, and *Spitzer*) photometry with a library of stellar population synthesis models to simultaneously determine the stellar mass, population age, and redshift with our own software. Our model grid consists of a four dimensional parameter space spanned by redshift (z), stellar population age[23] (t), V-band extinction (A_V), and star formation timescale (τ) for an exponentially declining star formation history. We assume solar metallicity, a Salpeter initial mass function, and adopt the CB07 population synthesis models. The allowed photometric redshifts ranged from $0 \leq z < 7$ with $\Delta z = 0.01$, the ages adopted by Bolzonella, Miralles, & Pelló (2000), extinctions of $0 \leq A_V \leq 2$ mag with $\Delta A_V = 0.2$ mag, and star formation timescales of $\tau \in [10^{-3}, 1, 2, 3, 5, 15, 30, 10^3]$ Gyr. We include a systematic uncertainty on the observed fluxes of the form $\sigma_f = \alpha \times f$, where we adopt $\alpha = 0.1, 0.1, 0.2$, and 0.2 for the ACS, WFC3, *VLT*, and *Spitzer* data, respectively to account for uncertainties in the zeropoints, templates, and measurement approach (whether `SExtractor` or `GalFit`, for the *HST* or *VLT/Spitzer* data). We compute the 1σ uncertainties on the stellar population parameters (e.g. mass, age, etc.) by use of a simple Monte Carlo calculation. For each band for a given galaxy, we draw a normal random variable with mean and standard deviation equal to the flux and flux uncertainty (without the the systematic term). By repeating for many iterations, we build up a distribution of each stellar population parameter and take the mean and standard deviation as the measured quantity and 1σ uncertainties, respectively.

We apply this approach to the complete sample of 30 BzH galaxies. In Figure 5, we show the photometric redshift distribution and the comparison to a spectroscopic redshift, when available. As expected, the median redshift of the sample is $z_{\rm phot} = 1.6 \pm 0.6$, where the uncertainty reflects the standard deviation of the distribution. To estimate our typical redshift uncertainty, we compare to the published spectroscopic redshifts in the lower panel of Figure 5. Based on the root-mean squared scatter of the seven objects with known spectroscopic redshifts, we estimate our uncertainties in $(1 + z)$ are $\sim 4.6\%$. We do recover the known galaxy cluster at

---

[23] We impose the usual self-consistency constraint that the a galaxy be younger than the age of the Universe.

TABLE 2
BzH GALFIT RESULTS

ID	r_e (arcsec)	$n^{\dagger}$	χ^2_{ν}	$F^{\ddagger}$	Notes
408	0.04 ± 0.00	4.72 ± 0.45	0.487	0.160	$\cdots$
606	0.09 ± 0.01	6.92 ± 0.92	0.404	0.158	$\cdots$
1696	0.41 ± 0.02	1.21 ± 0.10	0.356	0.170	$\cdots$
2227	0.35 ± 0.01	2.93 ± 0.09	0.364	2.517	$\cdots$
2377	0.16 ± 0.01	4.17 ± 1.01	0.322	0.049	$\cdots$
2749	0.51 ± 0.02	0.57 ± 0.05	1.849	0.191	$\cdots$
2750	1.03 ± 0.19	5.65 ± 0.58	1.891	0.591	$\cdots$
2871	0.03 ± 0.00	8.00 ± 2.76	0.567	0.023	unresolved
3000	0.60 ± 0.01	8.00 ± 0.14	0.814	9.440	tidal tail
3152	0.14 ± 0.00	4.66 ± 0.12	0.515	3.323	$\cdots$
3237	0.22 ± 0.01	7.54 ± 0.30	0.432	2.268	$\cdots$
3360	0.11 ± 0.00	7.58 ± 0.46	0.466	1.382	$\cdots$
3376	0.15 ± 0.01	2.21 ± 0.44	0.349	0.054	$\cdots$
3471	0.08 ± 0.00	4.40 ± 0.16	0.478	1.525	$\cdots$
3551	0.44 ± 0.01	2.74 ± 0.11	0.614	0.851	additional nuclear point source was fit
3812	0.16 ± 0.00	3.12 ± 0.07	0.486	3.767	$\cdots$
4148	0.04 ± 0.00	5.73 ± 0.32	0.443	0.690	$\cdots$
4173	0.37 ± 0.00	0.98 ± 0.02	0.359	2.373	$\cdots$
4324	0.25 ± 0.00	3.27 ± 0.08	0.404	4.536	$\cdots$
4327	0.03 ± 0.02	2.96 ± 3.62	0.411	0.000	unresolved
4534	0.14 ± 0.00	2.21 ± 0.07	0.388	2.718	$\cdots$
4648	0.17 ± 0.00	2.08 ± 0.10	0.355	0.913	$\cdots$
4846	0.16 ± 0.00	1.30 ± 0.13	0.506	0.232	$\cdots$
4921	0.19 ± 0.08	8.00 ± 4.50	0.337	0.012	unresolved
5410	0.00 ± 1.00	2.64 ± 1.00	0.364	-0.009	likely three distinct clumps
5529	0.29 ± 0.00	2.63 ± 0.12	0.369	1.107	$\cdots$
5685	0.48 ± 0.00	0.36 ± 0.02	0.386	1.399	$\cdots$
5735	0.08 ± 0.01	8.00 ± 4.15	0.349	0.012	unresolved
6845	0.42 ± 0.01	1.33 ± 0.04	0.385	1.648	$\cdots$
7202	0.30 ± 0.00	2.29 ± 0.04	0.434	5.825	$\cdots$

†The Sérsic index in equation (3).

‡The fractional difference between the goodness-of-fit for the PSF and Sérsic models (see § 4.1 for more details).
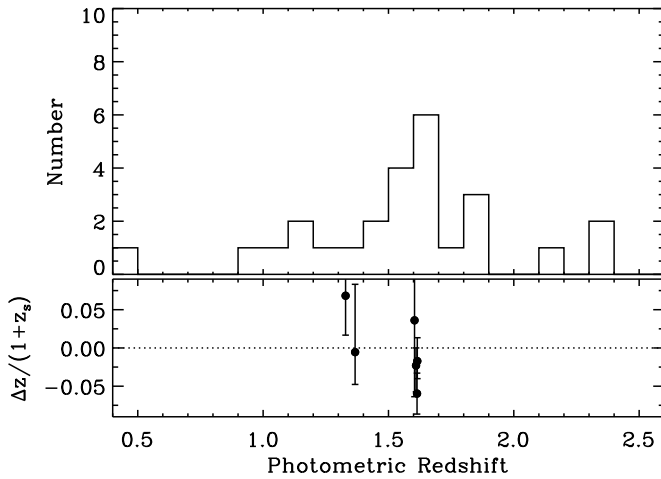

FIG. 5.— Photometric redshift distribution. In the upper panel, we show the photometric redshift distribution derived by the procedure described in § 4.3. As expected, our sample of BzH galaxies is generally located at $z_{\mathrm{phot}} = 1.6$. In the lower panel, we show the fractional difference between our redshift estimates and spectroscopic redshifts, where available. Based on the RMS on the fractional differences, we estimate that $(1 + z)$ is accurate to $\sim 4.6\%$.

$z \sim 1.6$ (Kurk et al. 2009). We present our resulting photometric redshifts and stellar population parameters in Table 3.

5. BZH GALAXY SIZE EVOLUTION

Based on the photometric redshift estimates and the spectroscopic data (where available), the BzH selection reliably identifies galaxies in the interval $\langle z \rangle \sim 1.6 \pm 0.6$. However to study the evolution of their sizes with redshift, we must compare to other similarly selected samples. The high redshift ($z \gtrsim 1.5$) samples are generally derived from similar color criteria presented here, and have effective radii measured in the H-band, for a rest frame wavelength of $\lambda_{\mathrm{rest}} \sim 6500$ Å. To ensure fair comparisons with lower redshift samples, we require similar rest frame sizes. For the low redshift data, we use the sample of 8666 early-type galaxies at $z \sim 0.2$ with effective radii measured in the i'-band (Bernardi et al. 2003) selected from the Sloan Digital Sky Survey, Early Data Release (SDSS-EDR; York et al. 2010). The stellar masses for the 7th Data Release[24] galaxies were determined following Salim et al. (2007). By cross matching these samples, we obtain 8595 galaxies for our low-redshift comparison. We select three mass ranges which are volume-limited based on the upper and lower flux limits imposed by detector saturation in SDSS and the Bernardi et al. (2003) brightness criterion. In Figure 6 we show these volume-limited selections (black boxes) and the flux limits (dashed lines). If these limits are not

[24] Obtained from http://www.mpa-garching.mpg.de/SDSS/DR7/.

TABLE 3
PHOTOMETRIC REDSHIFTS AND STELLAR POPULATION
PARAMETERS

ID	$z_{\rm phot}$	$z_{\rm spec}$	Age[†] (Gyr)	$M_*^{[‡]}$ ($10^{11}\ M_\odot$)	χ^2_ν
408	$1.59^{+0.05}_{-0.04}$	$\cdots$	$0.5^{+0.0}_{-0.0}$	0.4 ± 0.0	1.5
606	$1.87^{+0.24}_{-0.20}$	$\cdots$	$0.7^{+0.3}_{-0.2}$	0.4 ± 0.0	3.2
1696	$4.12^{+0.56}_{-3.58}$	$\cdots$	$0.4^{+3.1}_{-0.2}$	11.3 ± 1.1	2.4
2227	$1.27^{+0.11}_{-0.13}$	$\cdots$	$4.5^{+1.0}_{-1.0}$	1.3 ± 0.1	5.0
2377	$2.36^{+0.13}_{-0.54}$	$\cdots$	$0.5^{+3.0}_{-0.4}$	0.1 ± 0.0	0.6
2749	$1.85^{+0.27}_{-0.09}$	$\cdots$	$0.1^{+0.0}_{-0.0}$	0.8 ± 0.0	6.0
2750	$1.87^{+0.11}_{-0.09}$	$\cdots$	$0.5^{+0.2}_{-0.4}$	0.8 ± 0.0	8.4
2871	$1.54^{+0.08}_{-0.09}$	$\cdots$	$0.7^{+0.0}_{-0.4}$	0.2 ± 0.0	1.9
3000	$1.15^{+0.42}_{-0.04}$	$\cdots$	$5.5^{+0.0}_{-5.0}$	5.1 ± 0.2	4.1
3152	$1.38^{+0.21}_{-0.10}$	1.367	$4.5^{+0.0}_{-3.5}$	2.7 ± 0.1	0.3
3237	$1.66^{+0.08}_{-0.06}$	1.615	$0.7^{+0.0}_{-0.2}$	1.1 ± 0.1	4.0
3360	$1.63^{+0.44}_{-0.09}$	$\cdots$	$1.0^{+1.0}_{-0.5}$	1.2 ± 0.1	1.4
3376	$1.49^{+0.09}_{-0.11}$	$\cdots$	$0.3^{+0.5}_{-0.1}$	0.1 ± 0.0	4.3
3471	$1.67^{+0.06}_{-0.09}$	1.610	$1.0^{+0.0}_{-0.3}$	0.7 ± 0.0	2.5
3551	$1.60^{+0.06}_{-0.10}$	$\cdots$	$1.0^{+0.4}_{-0.3}$	2.2 ± 0.1	0.3
3812	$1.77^{+0.07}_{-0.07}$	1.614	$1.0^{+0.0}_{-0.0}$	1.0 ± 0.0	4.9
4148	$2.38^{+0.07}_{-0.05}$	$\cdots$	$0.4^{+0.0}_{-0.0}$	1.3 ± 0.1	2.8
4173	$0.98^{+0.31}_{-0.67}$	$\cdots$	$3.5^{+6.0}_{-2.1}$	0.3 ± 0.0	4.8
4324	$1.55^{+0.10}_{-0.09}$	$\cdots$	$1.0^{+0.4}_{-0.3}$	0.9 ± 0.0	2.5
4327	$3.15^{+1.10}_{-0.77}$	$\cdots$	$0.2^{+2.1}_{-0.1}$	1.9 ± 0.2	2.3
4534	$1.51^{+0.17}_{-0.26}$	1.604	$1.4^{+3.1}_{-0.4}$	0.9 ± 0.0	2.8
4648	$0.41^{+0.61}_{-0.10}$	$\cdots$	$8.5^{+1.0}_{-7.1}$	0.0 ± 0.0	2.8
4846	$1.63^{+0.10}_{-0.30}$	$\cdots$	$0.5^{+4.0}_{-0.3}$	0.3 ± 0.0	7.1
4921	$3.37^{+1.38}_{-1.69}$	$\cdots$	$0.7^{+2.8}_{-0.5}$	2.3 ± 0.3	2.0
5410	$2.12^{+0.17}_{-0.37}$	$\cdots$	$0.4^{+3.1}_{-0.3}$	0.2 ± 0.0	7.9
5529	$1.03^{+0.24}_{-0.35}$	$\cdots$	$4.5^{+3.0}_{-3.5}$	0.4 ± 0.0	3.5
5685	$1.41^{+0.13}_{-0.14}$	$\cdots$	$1.4^{+1.2}_{-0.4}$	0.2 ± 0.0	9.3
5735	$2.64^{+0.31}_{-0.15}$	$\cdots$	$0.3^{+2.0}_{-0.2}$	0.1 ± 0.0	3.0
6845	$1.67^{+0.64}_{-0.37}$	$\cdots$	$2.6^{+1.9}_{-1.9}$	0.9 ± 0.1	5.2
7202	$1.17^{+0.11}_{-0.12}$	1.329	$2.6^{+2.9}_{-0.3}$	1.7 ± 0.1	2.0

[†]Population age assuming an exponetial star formation history.
[‡]Stellar mass.

strictly imposed, then an artificial redshift dependence on the effective radii will be introduced as the radii are tightly correlated with the stellar masses, which roughly scale with luminosity. For example, without these volume limits, the effective radii of the SDSS galaxies will seem to *increase* with redshift since the survey is not sensitive to the lower mass (smaller) galaxies at the higher redshifts. Eliminating this potential Malmquist-like bias in the low redshift sample ensures a fair comparison between the high and low redshift data.

To investigate the passively evolving galaxy size evolution at a fixed stellar mass, we show in Figure 7 the effective radii as a function of redshift for this work (large circles), the SDSS sample (small dots), Longhetti et al. (2007, diamonds), Damjanov et al. (2009, triangles), Rutkowski et al. (2010, crosses), Daddi et al. (2005, asterisks), and Cimatti et al. (2008, squares). We overplot the two canonical models of $(1+z)^{-\alpha}$ (solid line) and $H(z)^{-\beta}$ (dot-dashed line), where $H(z)$ is the Hubble parameter, and present the best fit parameters in Table 4. While the data do not significantly favor either model, they serve to highlight an important trend: the amount by which galaxies are smaller in the past depends on the
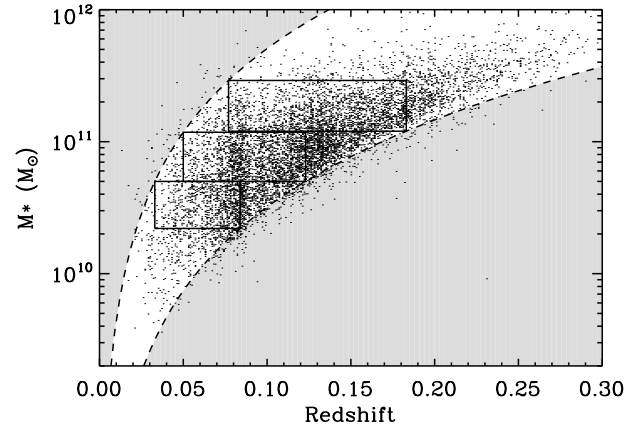

FIG. 6.— Selection of SDSS galaxy sample. We show the stellar mass as a function of spectroscopic redshift for the early-type galaxy sample of Bernardi et al. (2003) drawn from the SDSS-EDR. The stellar mass estimates were derived from stellar population fits to the SDSS photometry (Salim et al. 2007), and are similar in nature to those described in § 4.3. The dashed lines indicate the bright ($i' \leq 14$ mag) and faint ($i' \geq 17$ mag) completeness limits set by detector saturation and the Bernardi et al. (2003) selection, respectively. The boxes show our volume-limited selections for proper low-redshift comparisons. If such limits are not imposed, then an artificial trend in effective radius with redshift will arise from a Malmquist-type bias.

TABLE 4
MASS-DEPENDENT SIZE EVOLUTION MODELS

$\log M_{\rm low}$ ($\log M_\odot$)	$\log M_{\rm high}$ ($\log M_\odot$)	$\alpha^{[†]}$	$\beta^{[‡]}$	$R_e(z=0)$ (kpc)
10.3	10.7	0.38	0.49	2.76
10.7	11.1	0.87	1.07	4.36
11.1	11.5	1.42	1.86	7.60

[†]For the $(1+z)^{-\alpha}$ model.
[‡]For the $H(z)^{-\beta}$ model.

stellar mass. Newman et al. (2010) identified a similar result for 12 galaxies with dynamical masses determined from measured velocity dispersions.

Our stellar mass-dependent size evolution model is qualitatively similar to that proposed by Hopkins et al. (2009), where the power-law index varies with mass as $\alpha(M_*) \approx 0.23 \log\left(M_*/10^9\ M_\odot\right)$. However, their model underpredicts our measured power-law indices in our three mass regimes, but does give the same qualitative steepening of α with mass. Following their approach, we derive tentative relationships for the power-law indices:

$$\alpha(M_*) \approx -1.8 + 1.4 \times \log\left(\frac{M_*}{10^9\ M_\odot}\right) \qquad (5)$$

$$\beta(M_*) \approx -2.3 + 1.8 \times \log\left(\frac{M_*}{10^9\ M_\odot}\right), \qquad (6)$$

and caution that with only three independent mass bins, these fits should be considered preliminary at best. However, these results give indices consistent with the reported value of Buitrago et al. (2006), who find that $\alpha(M_* > 10^{11}\ M_\odot) \approx 1.5$.
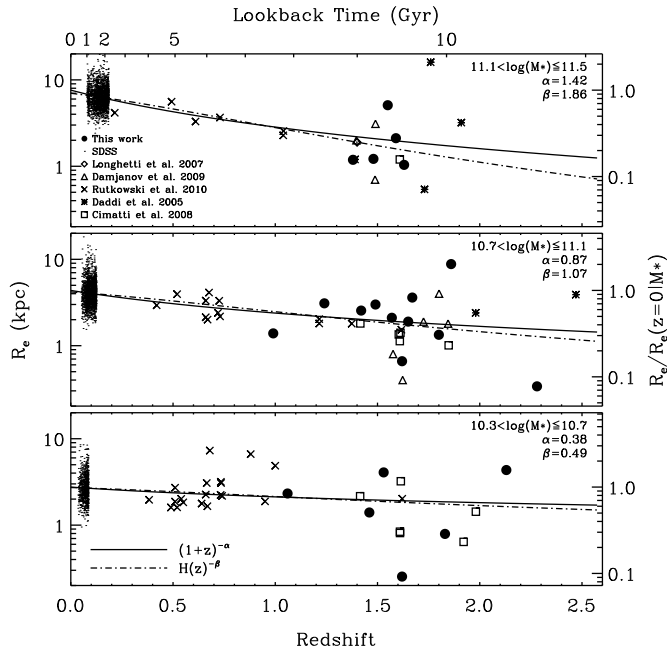
6. DISCUSSION

FIG. 7.— *BzH* galaxy size evolution. We show the effective radius versus redshift for the various stellar mass slices described in Figure 6 and several early-type galaxy samples. We do not show the uncertainties for clarity. As solid and dashed lines we show the best fit model of $R_e \propto (1 + z)^{-\alpha}$ and $R_e \propto H(z)^{-\beta}$, respectively. While the data cannot rule out either model, we show both to help illustrate the emerging trend: the increase in effective radii from $z \sim 2.5$ to present is strongest in high mass galaxies ($M^* \geq 10^{11}\ M_\odot$). Based on these fits, we give a tentative estimate for $\alpha(M_*)$ and $\beta(M_*)$ in equations (5) and (6), respectively.

It has become relatively well established that early-type galaxies are indeed smaller at high redshift than their local counterparts for a given stellar or dynamical mass (e.g. Trujillo et al. 2009; Newman et al. 2010). However the causes for this result are far less clear, or agreed upon. The likely mechanisms can be broadly characterized as astrophysical effects (early time major mergers, late time minor mergers, adiabatic expansion, or stellar mass-to-light gradients), or observational biases (underestimating the effective radii, overestimating the stellar masses, or incorrectly assuming that the high and low redshift populations are directly comparable). Using a semi-analytical model, Hopkins et al. (2010a) find that the factor of ~ 5 increase in the effective radii over the last ~ 10 Gyr for galaxies with $M_* \geq 10^{11}\ M_\odot$ can be explained by a combination these effects, with the late-time minor merging playing the largest role. However, we find that lower mass systems exhibit notably weaker redshift evolution, suggesting a different mixture of the main processes may be at work. For example, the adiabatic expansion mode may become more critical given the shallower gravitational potentials in the low mass systems.

As noted above, the *stellar mass-dependent size evolution* seen here is similar to the findings of Newman et al. (2010) for dynamical masses estimated from velocity dispersions, and has an interesting consequence for the $R_e - M_*$ relation. Shen et al. (2003) find that SDSS elliptical galaxies follow the scaling relation $R_e = R_{e,11}(M_*/10^{11}\ M_\odot)^\gamma$, where $R_{e,11} = 4.16$ kpc and $\gamma = 0.56$. However the mass-dependent size evolution ob-

served here and by Newman et al. (2010) imply either a fundamental change in the $R_e - M$ scaling relationship at high redshift (such as a flattening of the effective radius for decreasing stellar mass) or a redshift dependent value of γ, in addition to the usual lower value of $R_{e,11}$. However, at this stage the high redshift data cannot distinguish these two scenarios or shed light on the cause for this change.

The red galaxy formation paradigm wherein mergers of gas-rich discs trigger intense starbursts which are later quenched by active galactic nuclei, finally giving way to dead spheroidal systems spent of their gas (e.g. Faber et al. 2007, and references therein) suggests the passive galaxies may have come from a population of more active galaxies in their recent past. The Lyman-break galaxies (LBGs) observed at $z \gtrsim 3$ are a possible progenitor system. While their stellar masses are far less well constrained due to the lack of rest frame IR data, the majority of LBGs have $M_* \sim 10^{10}\ M_\odot$ between $3 \lesssim z \lesssim 6$ (e.g. Papovich, Dickinson, & Ferguson 2001; Yan et al. 2006). Therefore, the typical LBG at $3 \lesssim z \lesssim 6$ belongs in the lower panel of Figure 7, and have effective radii of $R_e \sim 1$ kpc (e.g. Ferguson et al. 2004; Bouwens et al. 2006; Hathi, Malhotra, & Rhoads 2008; Oesch et al. 2010), after transforming to an equivalent rest frame wavelength (Barden et al. 2005). The LBGs are then consistent with our $H(z)^{-\beta}$ model, possibly suggesting that the physical mechanism driving the passive galaxy evolution may be at work for the LBGs as well. Given their increased star formation rates, larger gas content, and lower total mass, the mass-loss modes, whether driven by AGN (e.g. Fan et al. 2008) or stellar winds (e.g. Damjanov et al. 2009), are likely more important. However, we recognize that these samples (LBGs and passive galaxies) are quite different and that the next generation of space-based infrared instruments (Near-Infrared Camera and Mid-Infrared Instrument on *James Webb Space Telescope*) will provide a much clearer picture for the high redshift ($z \gtrsim 3$) size comparisons.

7. SUMMARY

We identified 30 passively evolving galaxies to $H \leq 25$ mag from a set of color criteria similar to the pBzK selection. We measure rest frame optical ($\lambda_{\rm rest} \sim 6500$ Å) effective radii as two-dimensional fits to the H-band image. By comparing with several other comparable samples at various redshifts, we find that the size evolution depends on the stellar mass. We give tentative scalings between the power-law index of the $R_e - z$ relation and stellar mass. Future surveys, such as the coming Multi-Cycle Treasury programs with *HST*, will have the unique opportunity to improve upon our scalings and extend to both higher redshifts and lower stellar masses.

REFERENCES

Barden, M., et al. 2005, ApJ, 635, 959
Bell, E. F., et al. 2004, ApJ, 608, 752
Bell, E. F., et al. 2006, ApJ, 640, 241
Bernardi, M., et al. 2003, AJ, 125, 1817
Berin, E. & Arnouts, S. 1996, A&AS, 117, 393
Bolzonella, M., Miralles, J.-M., & Pelló, R. 2000, A&A, 363, 476
Bond, N. A., Gawiser, E., Gronwall, C., Ciardullo, R., Altmann, M., & Schawinski, K. 2009, ApJ, 705, 639
Bouwens, R. J., Illingworth, G. D., Blakeslee, J. P., & Franx, M. 2006, ApJ, 653, 53
Bremer, M. N., et al. 2006, MNRAS, 371, 1427
Brown, M. J. I., Dey, A., Jannuzi, B. T., Lauer, T. R., Tiede, G. P., & Mikles, V. J. 2003, ApJ, 597, 225
Brown, M. J. I., Dey, A., Jannuzi, B. T., Brand, K., Benson, A. J., Brodwin, M., Croton, D. J., & Eisenhardt, P. R. 2007, ApJ, 654, 858
Buitrago, F., Trujillo, I., Conselice, C. J., Bouwens, R. J., Dickinson, M., & Yan, H. 2008, ApJ, 687, L61
Calzetti, D., Kinney, A. L., & Storchi-Bergmann, T. 1994, ApJ, 429, 582
Charlot, S. & Bruzual, G. 2007, in prep
Cimatti, A., et al. 2004, Nature, 430, 184
Cimatti, A., Daddi, E., & Renzini, A. 2006, A&A, 453, L29
Cimatti, A., et al. 2008, A&A, 482, 21
Coleman, G. D., Wu, C.-C., & Weedman, D. W. 1980, ApJS, 43, 393
Cox, T. J., Di Matteo, T., Hernquist, L., Hopkins, P. F., Robertson, B., & Springel, V., 2006, ApJ, 650, 791
Daddi, E., Cimatti, A., Renzini, A., Fontana, A., Mignoli, M., Pozzetti, L., Tozzi, P., & Zamorani, G. 2004, ApJ, 617, 746
Daddi, E., et al. 2005, ApJ, 626, 680
Damjanov, I., et al. 2009, ApJ, 695, 101
Demarco, R., et al. 2010, ApJ, 711, 1185
Dickinson, M., et al. 2004, ApJ, 600, L99
Djorgovski, S. & Davis, M. 1987, ApJ, 313, 59
Dressler, A., Lynden-Bell, D., Burstein, D., Davies, R. L., Faber, S. M., Terlevich, R., & Wegner, G. 1987, ApJ, 313, 42
Eggen, O. J., Lynden-Bell, D., & Sandage, A. R. 1962, ApJ, 136, 748
Faber, S. M., et al. 2007, ApJ, 665, 265
Fan, L., Lapi, A., de Zotti, G., & Danese, L. 2008, ApJ, 689, L101
Ferguson, H. C., et al. 2004, ApJ, 600, L107
Giavalisco, M., et al. 2004, ApJ, 600, L93
Glazebrook, K., et al. 2004, Nature, 430, 181
Hathi, N. P., Malhotra, S., & Rhoads, J. E. 2008, ApJ, 673, 686
Hopkins, P. F., Hernquist, L., Cox, T. J., Keres, D., & Wuyts, S. 2009, ApJ, 691, 1424
Hopkins, P. F., Bundy, K., Hernquist, L., Wuyts, S., & Cox, T. J. 2010, MNRAS, 401, 1099

Hopkins, P. F., et al. 2010, ApJ, 715, 202
Kalirai, J. S., et al. 2009a, Instrument Science Report WFC3, 2009-31
Kalirai, J. S., et al. 2009b, Instrument Science Report WFC3, 2009-30
Koekemoer, A. M., Fruchter, A. S., Hook, R. N., & Hack, W. 2002, hstc.conf, 337
Kormendy, J. 1977, ApJ, 218, 333
Kurk, J., et al. 2009, A&AS, 504, 331
Lane, K. P., et al. 2007, MNRAS, 379, L25
Longhetti, M., et al. 2007, MNRAS, 374, 614
Luo, B., et al. 2008, ApJS, 179, 19
Madau, P. 1995, ApJ, 441, 18
McCarthy, P. J., et al. 2004, ApJ, 614, L9
Naab, T., Khochfar, S., & Burkert, A. 2006, ApJ, 636, L81
Naab, T., Johansson, P. H., & Ostriker, J. P. 2009, ApJ, 699, L178
Newman, A. B., Ellis, R. S., Treu, T., & Bundy, K. 2010, ApJL, submitted
Oesch, P. A., et al. 2010, ApJ, 709, L16
Oke, J. B. & Gunn, J. E. 1983, ApJ, 266, 713
Papovich, C., Dickinson, M., & Ferguson, H. C. 2001, ApJ, 559, 620
Peng, C., Ho, L. C., Impey, C. D., & Rix, H.-W. 2002, AJ, 124, 266
Retzlaff, J., et al. 2010, A&A, 511, 50
Rudnick, G., et al. 2003, ApJ, 599, 847
Rutkowski, M. J., et al. 2010, ApJ, submitted
Salim, S., et al. 2007, ApJS, 173, 267
Saracco, P., Longhetti, M., & Gargiulo, A. 2010, MNRAS, accepted, arXiv: 1004.3403
Shen, S., Mo, H. J., White, S. D. M., Blanton, M. R., Kauffmann, G., Voges, W., Brinkmann, J., & Csabai, I. 2003, MNRAS, 343, 978
Spergel, D. N., et al. 2003, ApJS, 148, 175
Trujillo, I., et al. 2006, MNRAS, 373, L36
Trujillo, I., Cenarro, A. J., de Lorenzo-Cáceres, A., Vazdekis, A., de la Rosa, I. G., & Cava, A. 2009, ApJ, 692, L118
van Dokkum, P. G. 2005, AJ, 130, 2647
van Dokkum, P. G., et al. 2008, ApJ, 677, L5
van Dokkum, P. G. & Brammer, G. 2010, ApJ, submitted, arXiv: 1003.3446
Windhorst, R. A., et al. 2010, ApJS, arXiv: 1005.2776
Yan, H., Dickinson, M., Giavalisco, M., Stern, D., Eisenhardt, P. R. M., & Ferguson, H. C. 2006, ApJ, 651, 24
York, D. G., et al. 2000, AJ, 120, 1579